

Geophysical Research Letters®


RESEARCH LETTER

10.1029/2021GL094519

Special Section:

Years of the Maritime
Continent

The Oceanic Barrier Layer in the Eastern Indian Ocean as a Predictor for Rainfall Over Indonesia and Australia

Detelina P. Ivanova¹ , Julie L. McClean¹ , Janet Sprintall¹ , and Ru Chen^{1,2} 

¹Scripps Institution of Oceanography, UCSD, La Jolla, CA, USA, ²School of Marine Science and Technology, Tianjin University, Tianjin, China

Key Points:

- Salt-stratified barrier layers can influence sea surface temperature and hence the coupled air-sea exchanges
- Barrier layers in the east Indian Ocean warm pool are significantly correlated to the terrestrial rainfall in Australia and Indonesia
- Thick barrier layers intensify evaporation and amplify the moisture transported to Australia, increasing rainfall

Supporting Information:

Supporting Information may be found in the online version of this article.

Correspondence to:

J. Sprintall,
jsprintall@ucsd.edu

Citation:

Ivanova, D. P., McClean, J. L., Sprintall, J., & Chen, R. (2021). The oceanic barrier layer in the eastern Indian Ocean as a predictor for rainfall over Indonesia and Australia. *Geophysical Research Letters*, 48, e2021GL094519. <https://doi.org/10.1029/2021GL094519>

Received 2 JUN 2021

Accepted 29 OCT 2021

Author Contributions:

Conceptualization: Janet Sprintall
Data curation: Detelina P. Ivanova
Formal analysis: Detelina P. Ivanova
Funding acquisition: Julie L. McClean, Janet Sprintall
Investigation: Detelina P. Ivanova
Methodology: Detelina P. Ivanova, Janet Sprintall, Ru Chen
Resources: Julie L. McClean
Software: Detelina P. Ivanova, Ru Chen
Supervision: Julie L. McClean, Janet Sprintall
Validation: Detelina P. Ivanova
Visualization: Detelina P. Ivanova

Abstract Barrier layers in the tropics trap heat in a shallow and stable near-surface layer and limit entrainment of cooler water from below. Both processes act to increase sea surface temperature and enhance atmospheric convection. The high resolution fully coupled pre-industrial Energy Exascale Earth System Model version 0 (E3SMv0) is used to investigate the relationship between barrier layers in the eastern Indian Ocean during the wet season with local atmospheric convection and remote rainfall. A partial least squares regression reveals a significant relationship between Australasian rainfall and the barrier layer thickness (BLT) west of Sumatra, occurring one month earlier. The largest positive regression coefficients are over northern Australia. The region west of Sumatra is strategically located where the East-Asian monsoon moisture flows toward northern Australia. Thickening of the west Sumatra BLT intensifies evaporation and local convection and amplifies the moisture transported to Australia acting to increase the terrestrial rainfall.

Plain Language Summary Strong salinity stratification at the base of a surface mixed layer can act as a barrier for the heat exchange between the surface and the deep ocean. Thick barrier layers occur in November-January in the region west of Sumatra, Indonesia, warming the upper ocean and intensifying the local rainfall through air-sea interaction. This actively contributes to the water moisture transported by the monsoons throughout the tropical Indo-Pacific region. Thus, oceanic barrier layers offshore of Sumatra in the eastern Indian Ocean play an important role in the prediction of seasonal, terrestrial rainfall over the Indonesian-Australian region.

1. Introduction

The predictability of rainfall is of great importance to the communities living in monsoon areas such as Indonesia and northern Australia where seasons alternate between wet and dry. However, while the Indonesian Maritime Continent features the world's largest rainfall with rates of about 2,700 mm/year (Yamanaka et al., 2018), the Australian continent is one of the most arid zones in the world; during the catastrophic Millennium Drought, (1997–2005) precipitation rates were less than 200 mm/year (Freund et al., 2017). In a time of changing climate and growing population, extreme events like torrential rainfall and prolonged drought have increasing socio-economic impacts that demand improved forecasts of precipitation. A prime example is the unprecedented 2019–2020 bushfire season in Australia (Abram et al., 2021; van Oldenborgh et al., 2020) that occurred in the third year of anomalously dry conditions across much of the continent.

Rainfall over the Indonesian archipelago and Australian Continent (IAAC) is related to the sea surface temperature (SST) variability in both the Pacific and Indian Ocean associated with the El-Niño Southern Oscillation (ENSO), the Indian Ocean Dipole (IOD), the Madden-Julian Oscillation (MJO), the Southern Annular Mode (SAM), and atmospheric blocking (Choudhury et al., 2017; Meyers et al., 2007; Nicholls, 1989; Risbey et al., 2009; Wheeler et al., 2009). Positive IOD and El Niño events are connected to increased drought conditions over Australia and vice-versa for negative IOD and La Niña (Meyers et al., 2007; Risbey et al., 2009). A “basin wide warming” Indian Ocean SST mode extends the dry conditions over Australia after the decay of an El Niño (Taschetto et al., 2011). Possible mechanisms for such large-scale teleconnections are barotropic atmospheric Rossby wave trains generated during the wind shifts of the monsoon transition as well as the poleward transport of IOD and ENSO associated equatorial heat anomalies (Cai et al., 2011).

Over the Indonesian Maritime Continent, monsoon dynamics is complicated by complex island coastlines and orography, land-sea contrasts, and air-sea interaction (Chang et al., 2016; Robertson et al., 2011;

Writing – original draft: Detelina P. Ivanova

Writing – review & editing: Julie L. McClean, Janet Sprintall, Ru Chen

Yamanaka et al., 2018). Yamanaka et al. (2018) suggested two major annual precipitation cycle regimes: the southern-hemisphere section (e.g., Java) has a distinct annual cycle with the rainfall maximum occurring in the austral summer and the minimum in austral winter, while the equatorial and northern-hemisphere sections (e.g., North Sumatra) have a semi-annual regime with no distinct dry season. The interannual variability of the Indonesian Maritime Continent rainfall is dominated by ENSO over its central and eastern regions and by the IOD in its western regions (Aldrian & Susanto, 2003; Hamada et al., 2002; Hendon, 2003; Hidayat et al., 2016).

While SST variability has shown clear links to regional rainfall and wind patterns, the role that salinity stratification might play in driving regional climate variability is less clear since there is no obvious direct mechanism for salinity itself to induce climate patterns. A few recent studies have examined the relationship of sea surface salinity (SSS) to terrestrial rainfall (e.g., Li et al., 2016a, 2016b; Rathore et al., 2020). Positive SSS anomalies are mostly associated with anomalous atmospheric moisture flux divergence over the ocean that carries the excessive moisture to the surrounding continents where it precipitates. Rathore et al. (2020) found robust correlation patterns between the Australian rainfall and high/low SSS anomalies in the equatorial Indo-Pacific associated with the divergence/convergence of the atmospheric moisture flux over Australia. While the SSS anomalies provide a fingerprint of anomalous moisture flux convergence, salinity stratification can also feedback to air-sea interaction in the boundary layer. For example, salinity-stratified barrier layers trap heat in a warm surface layer that can impact SST variability (e.g., Drushka et al., 2014; Li et al., 2016; Krishnamohan et al., 2019; Mahadevan et al., 2016; Li et al., 2017) or intensify the surface turbulent heat fluxes due to enhanced wind forcing (Pujiana & McPhaden, 2018). These barrier layer impacts on the coupled air-sea exchange and links to atmospheric advection can occur over a range of time scales including subseasonal (Drushka et al., 2014; Pujiana & McPhaden, 2018) to seasonal (Felton et al., 2014; Masson et al., 2002). Barrier layers occur where large amounts of precipitation produce a strong freshwater influx at the ocean surface and consequently create strong salinity stratification (Sprintall & Roemmich, 1999; Sprintall & Tomczak, 1992). The region west of Sumatra, located in the Indo-Pacific warm-fresh pool (Vinayachandran & Shetye, 1991), is associated with persistent barrier layer formation (Felton et al., 2014; Masson et al., 2002; Qiu et al., 2012; Sprintall & Tomczak, 1992). The zonal advection of fresh water from the Bay of Bengal or within the equatorial Wyrtki Jets may also enhance barrier layer formation in this region (Drushka et al., 2014; Masson et al., 2002).

Our study will test the hypothesis that the thickness of salt-stratified barrier layers in the eastern Indian Ocean is significantly related to rainfall over the IAAC. We focus on the region to the west of Sumatra where a persistent local maximum in barrier layer thickness occurs in the eastern Indian Ocean (Figure 1, black box). The main premise is that barrier layers in the region west of Sumatra both prevent entrainment of cooler water from below as well as trap surface heat in shallow but stable near-surface layers and so act to increase SST. In turn, atmospheric convection and consequently rainfall are enhanced over the IAAC.

2. Data and Methods

2.1. Observations

We use the monthly high-resolution precipitation data set (2000–2021) from the National Aeronautics and Space Administration (NASA) Integrated Multi-satellite Retrievals for GPM (Global Precipitation Measurements) version 6 (IMERGv6). It is a final level three merged product from the Tropical Rainfall Measuring Mission (TRMM) and the GPM international satellite constellation mission. This product combines high-quality microwave and infrared data, and rain gauge precipitation (Huffman et al., 2019). It is available on a 0.1° latitude \times 0.1° longitude grid with global coverage from 90°S to 90°N from 2000 to 2021. We use the monthly global $1^\circ \times 1^\circ$ optimally interpolated temperature and salinity profiles with 58 vertical levels (maximum depth 2000 db) derived from Argo floats (2004–2017; Roemmich & Gilson, 2009). The first vertical level at 2.5 db is used for SST and SSS. In addition, we use the Advanced Microwave Scanning Radiometer 2 (AMSAR-2) SST monthly (2013–2020) product version 8.2 that is on a 0.25° global grid and represents a foundation SST at a depth of ~ 1 m (Wentz et al., 2014). QuikSCAT scatterometer climatology of ocean winds (SCOW) on a 0.25° latitude \times 0.25° longitude global grid are used from the period 1999–2007 (Risien & Chelton, 2008).

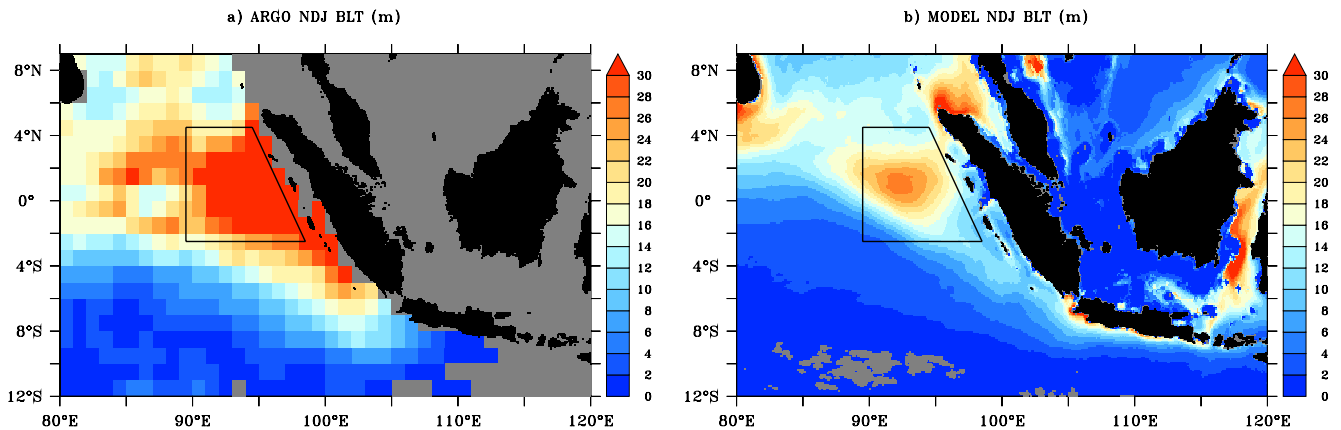


Figure 1. Barrier layer thickness (m) distribution in Nov-Dec-Jan from (a) Argo profiles (1998–2016) and the (b) Pre-Industrial (PI) E3SM v0 model (years 85–131). The box outlines the West Sumatra (WS) study region.

2.2. Model

To test our hypothesis, we use a high-resolution fully coupled 1850 pre-industrial (constant greenhouse gas concentrations, particularly 284.7 ppmv for CO_2) climate model simulation carried out with the Energy Exascale Earth System Model (E3SMv0; McClean et al., 2018). This version of the model is largely based on the Community Earth System Model (CESM) version 1.3 (Meehl et al., 2019); its components include the Community Atmosphere Model version 5-Spectral Element (CAM5-SE), the Community Land Model version 4 (CLM4), the Los Alamos Parallel Ocean Program version 2 (POP2), and the Los Alamos sea ice model version 4 (CICE4). The nominal horizontal grid resolution is 0.25° in the atmosphere and land components and 0.1° in the ocean and sea ice components. The atmospheric model has 30 vertical hybrid levels. The cloud physics in CAM5-SE (Park et al., 2014) reduced known biases in total, mid-level and optically thick clouds (Kay et al., 2012) occurring in earlier model versions. In the ocean model, the vertical grid has 42 depth levels with variable thickness from 10 to 50 m in the upper 300 m. Sub-grid scale horizontal mixing processes are parameterized via biharmonic operators (Maltrud et al., 2010) for both momentum and tracers, and the K-Profile Parameterization (KPP) is used to represent vertical mixing (Large et al., 1994). The ocean and sea-ice model components were initialized from a two-year spun up state of a global 0.1° POP2/CICE4 simulation forced with interannually varying corrected Coordinated Ocean-ice Reference Experiments phase II (Large & Yeager, 2009) surface atmospheric fluxes (Li et al., 2014). The preindustrial simulation was integrated for 131 years; our study used only the last 47 years (years 85–131) to exclude the initial model adjustment period.

We constructed seasonal climatologies from the model monthly time series of ocean temperature and salinity profiles. The first vertical level at 5 m was used for SST and SSS. Atmospheric variables included the total precipitation, heat fluxes (net, latent and sensible heat fluxes at the surface), outgoing longwave radiation at the top of the atmosphere, wind stress, winds, the vertically integrated total moisture, and meridional moisture transport. The simulated large-scale indices Niño3.4 and the IOD were derived from the monthly SST time series. The Niño3.4 is the area averaged SST anomalies over the equatorial Pacific 5°S – 5°N , 120°W – 170°W (Trenberth, 1997). The IOD index is the difference of the area averaged SST anomalies between the two Indian ocean regions 10°S – 10°N , 50 – 70°E and 0° – 10°S , 90 – 110°E (Saji et al., 1999).

The fidelity of the model solution is examined below via comparison with observations and reasonable agreement is found in regional properties. In part, the differences are because the model results are from the pre-industrial period while the observed climatologies are from the industrial era. For example, long term observed trends show warming SST (Hurrell et al., 2008) and freshening SSS (Durack & Wijffels, 2010) of the eastern Indian Ocean; comparison of these with our pre-industrial model simulation would result in cooler and saltier differences. The simulation capabilities of standard climate models are challenged by the complex topography and air-sea-land interaction in the Indonesian Maritime Continent (Chang et al., 2016;

Neale & Slingo, 2003; Sperber et al., 2013). By using higher-resolution model components, the model topography is more realistic, and a broader range of interactions and feedbacks are simulated.

2.3. ILD, MLD, and BLT Definition

The barrier layer thickness (BLT) is the difference between the isothermal layer depth (ILD) and the mixed layer depth (MLD; i.e., $BLT = ILD - MLD$; Sprintall & Tomczak, 1992). The ILD is the depth at which the temperature is 0.5°C lower than the temperature at 10 m depth. The MLD is the depth at which the potential density increment from 10 m is equivalent to a temperature decrease of 0.5°C (Sprintall & Roemmich, 1999; Sprintall & Tomczak, 1992). These quantities were calculated using the model and the observational (Argo) temperature and salinity monthly time series.

2.4. Partial Least Square (PLS) Regression

We used the model output to investigate the relationship of the continental total precipitation in the IAAC to a set of ocean variables used as predictors in a lagged partial least square (PLS) regression (Rosipal & Kramer, 2006). Such a complex relationship is difficult to explore with existing observational data sets, which are sparse and inconsistent in space and time. In the PLS regression method, both predictors and the response variable are projected onto a plane of maximal correlation such that they explain the maximum variance possible for each variable. The PLS regression coefficients isolate the relationship between two variables after removing the combined effect from the rest of the variables. Previous studies have used partial correlations to study the rainfall relationships with Indian Ocean SST, ENSO and IOD (Nicholls, 1989; Risbey et al., 2009).

The ocean variables are from the region west of Sumatra where barrier layers are found on an annual basis. The West Sumatra (WS) box's western boundary runs from 2.5°S to 4.5°N and its southern and northern boundaries extend from 89.5°E to 98.5°E and 94.5°E, respectively (Figure 1, black box). Simulated monthly time series of WS box area-averaged standardized anomalies (divided by the standard deviation) of BLT, MLD, SST, and the large-scale climate indices of Niño 3.4 (ENSO3.4) and IOD, were used to construct the PLS regression fit of the monthly IAAC rainfall:

$$\text{Rain}(t+l) = b_0 + b_1 \cdot \text{SST}(t) + b_2 \cdot \text{MLD}(t) + b_3 \cdot \text{BLT}(t) + b_4 \cdot \text{ENSO34}(t) + b_5 \cdot \text{IOD}(t) \quad (1)$$

where t is time in months, l is time lag in months, and b_0 – b_5 are the regression coefficients to be determined. The WS SSS showed no significant correlation with IAAC rainfall and so was omitted from the PLS. The average decorrelation time scale for the five predictors is 2.36 months (see Text S1 in Supporting Information S1), so the PLS regressions were performed with lags of $l = 0, 1$ and 2 months prior to the rainfall time series. The largest BLT regression values were found after a lag of 1 month. Error bars for the predictor regression coefficients (b_i , where $i = 1, 5$) in Equation 1 at each point in the rainfall regression maps were estimated using a bootstrapping technique (Chernick, 2011) rather than by standard hypothesis testing due to the non-normal distributions of the rainfall and predictors (See Text S2 in Supporting Information S1).

3. Variability of the Upper Ocean in Eastern Equatorial Indian Ocean

Our focus is on the WS box (Figure 1) where the thickest barrier layers in the eastern Indian Ocean are found in both the Argo data and the simulation in November–January (NDJ) centered at ~95°E, 2°N. The BLT maxima stretches from ~85° to 90°E in the equatorial region to the coast of Sumatra and southward along the coast. The model simulates the observed climatological BLT spatial distribution well but underestimates the thickness. Possible explanations for this model bias may be that biased-weak equatorial winds lead to shallower mixed layers (Figure S1 in Supporting Information S1).

The Argo SSS annual cycle (Figure 2a) in the WS box shows salinities of 34–34.3 for most of the year decreasing to reach a minimum of 33.6 in October. The model does a reasonable job simulating this annual SSS evolution. Despite the pre-industrial period of the model, which should suggest a saltier state compared to the long-term observed freshening of the equatorial eastern Indian Ocean (Durack & Wijffels, 2010),

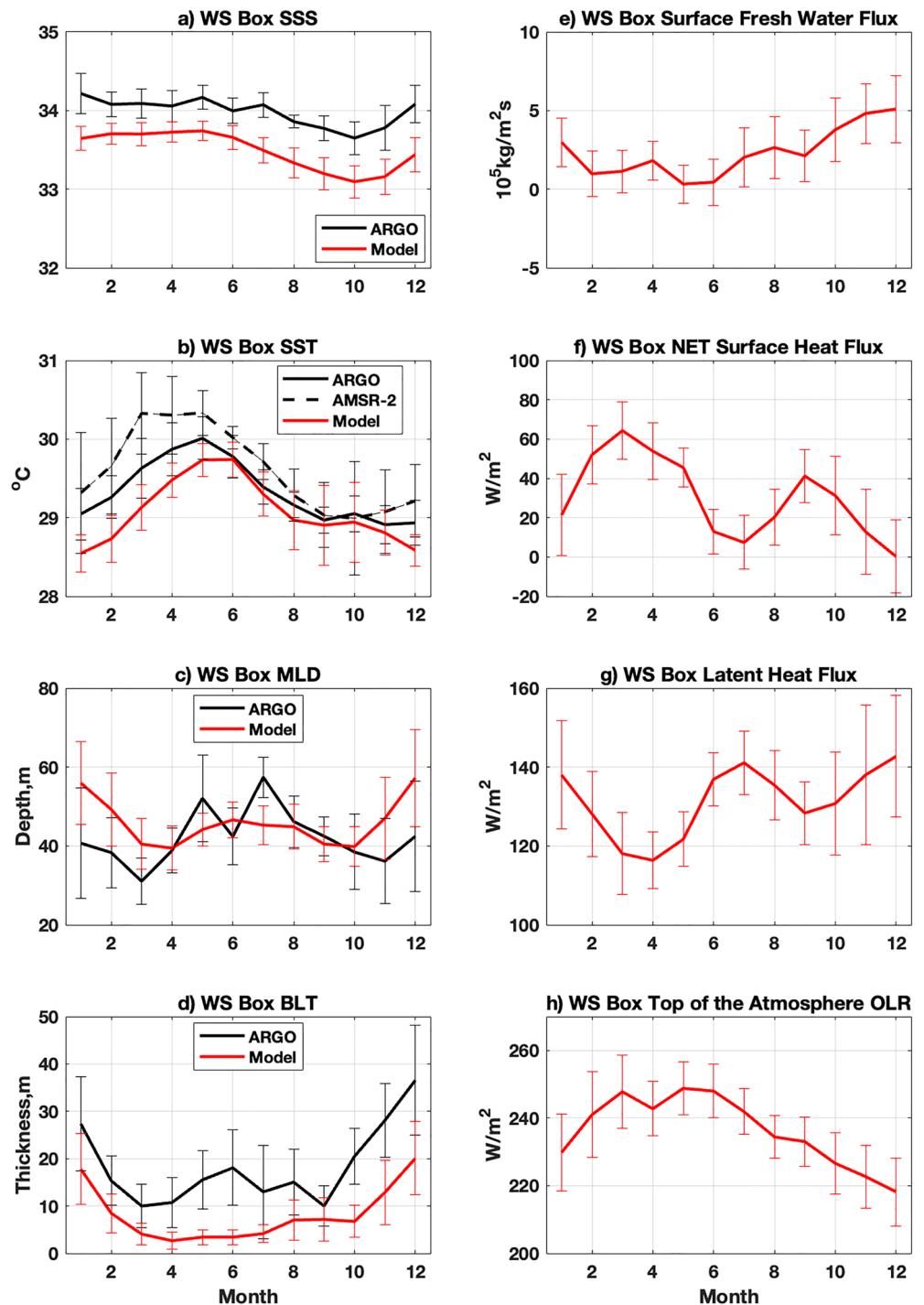


Figure 2. Mean (line) annual cycles and standard deviations (whiskers) of the WS area-averaged quantities from Argo (black lines) and PI E3SMv0 (red lines): (a) Sea surface salinity (SSS); (b) Sea surface temperature (SST, °C), the black dashed line is AMSR-2 SST observations; (c) Mixed layer depth (MLD, m); (d) Barrier layer thickness (BLT, m). PI E3SMv0 (e) Surface freshwater flux (kg/m²s); (f) Net surface heat flux (W/m²); (g) Latent heat flux (W/m²); (h) Outgoing longwave radiation (OLR, W/m²) at the top of the atmosphere.

in the WS box, the model exhibits a systematic fresh bias of ~ 0.5 with a lower salinity range of 33.2–33.6 compared to the Argo SSS observations. These lower salinity anomalies can be caused either by excessive precipitation or by low salinity advection. The simulated precipitation climatology is somewhat drier compared to the IMERG climatology (Figure S1 in Supporting Information S1) and a comparison of model and observations find the model's lower salinity anomalies that are advected into the area from the Bay of Bengal (not shown).

Observed SSTs in this equatorial region have only a small range of 28.8°–30°C (Figure 2b) as seen in the ARGO data, with slightly higher temperatures in the AMSR-2 product of 29°–30.3°C. The difference may be explained by the different periods of the two climatologies and the different SST representations at 2.5 m for the Argo product while the satellite measurements represent a foundation SST at a depth of 1 m. This temperature range is always favorable ($>27.5^\circ\text{C}$) for the development of atmospheric convection (Graham & Barnett, 1987). SST warms up by $\sim 1^\circ\text{C}$ from January to reach a maximum in May (30°C) and cools back down from September through January to 29°C. A similar SST annual cycle is seen in the model (Figure 2b) and agrees within one standard deviation, although the model tends to be cooler at the beginning and very end of the year.

The Argo MLD annual cycle varies from 30 to 60 m (Figure 2c), with the maximum occurring in July and two distinct minimums occurring during the monsoon transitions in March and November.

The model annual cycle is somewhat smoother than the observations (Figure 2c) being shallower in May and July and deeper in December–February (DJF). The MLD minima in the model appear 1 month later in the spring (April) and 1 month earlier in the fall (October) compared to the observations.

The Argo climatology shows the continuous presence of the barrier layer in the WS during the entire year with thicknesses of 10–40 m (Figure 2d). The simulated BLT is overall thinner (5–20 m) than the observed (Figures 1b and 2d), but the timing of the maximum thickness occurring in NDJ (Figure 2d) is well captured. This BLT maximum coincides with the period of increased net surface freshwater flux (Figure 2e) and reduced SSS (Figure 2a).

Thickening of the barrier layer during the year intensifies the surface turbulent heat fluxes resulting in increased evaporation and atmospheric convection (Figures 2f–2h). The season of thickest barrier layers (NDJ) in the WS coincides with a period of intensified East-Asian-Australian monsoon winds (with a southward meridional component, Figure S2d in Supporting Information S1) and surface cooling by both reduced incoming short-wave radiation (dominating the net surface energy balance, Figure 2f and Figure S2a in Supporting Information S1) and intensified heat loss by the turbulent heat fluxes (Figure 2g and Figure S2c in Supporting Information S1). The latent heat flux (Figure 2g) is the second major contributor (after shortwave radiation) to the net surface heat balance (~ 113 – 140 W/m^2), and its increase indicates intensified evaporation. At the same time, the OLR (often used as a proxy for atmospheric convection Webster et al., 1998) is at its annual minimum, evidence for intensified convection (Figure 2h). In contrast, during the monsoon transition seasons (e.g., March–May, MAM), when the barrier layer is thin, weakened wind forcing is accompanied by increased solar radiation warming and reduced turbulent fluxes and evaporation. In MAM, OLR is at its maximum indicating reduced convective activity. Collectively, these results concur with previous studies that reported that the barrier layer plays an important role intensifying the surface latent and sensible heat fluxes in the surface mixed layer during active phases of MJO (Drushka et al., 2014; Chi et al., 2014) and during the passage of atmospheric Kelvin waves (Pujiana & McPhaden, 2018). Our analysis suggests similar mechanisms occur during seasonal transitions of the winds.

4. The Impact of the Barrier Layer on Remote Rainfall Patterns

We investigate the connection between the barrier layer west of Sumatra and the remote rainfall over the IAAC during the wet season of DJF. First, we examine the fidelity of the E3SMv0 model precipitation distribution and compare the 21-year (2000–2021) IMERG seasonal rainfall in DJF (Figure 3a) with the model for years 85–131 (Figure 3b). The observed rainfall distribution features an almost zonal pattern with the driest areas in southern and western Australia and increasing rainfall to the north and east (Figure 3a). The local precipitation reaches a maximum rate of about 6–8 mm/day in the northern coastal area where

Rainfall PLS Regression

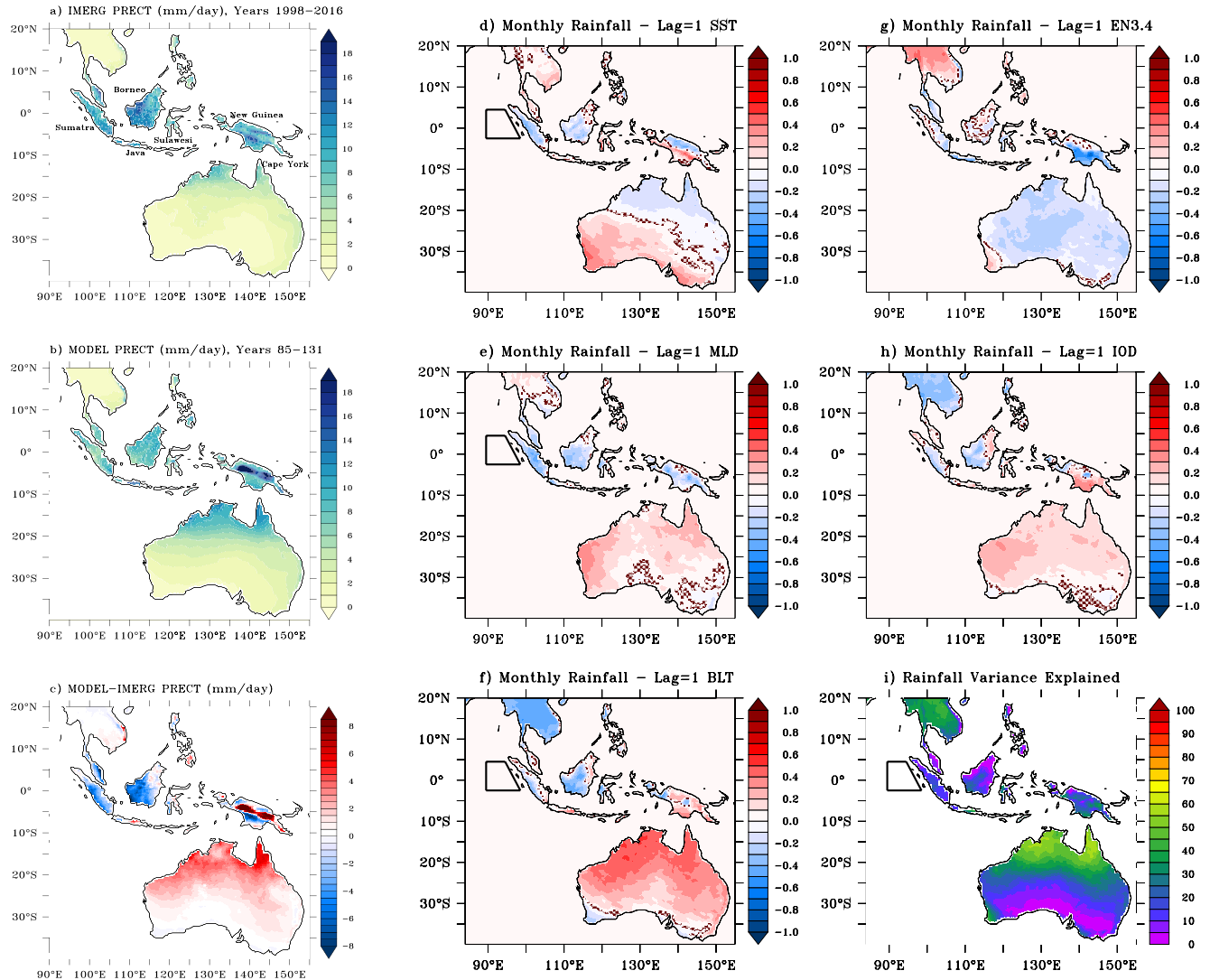


Figure 3. December–February (DJF) seasonal maps of total precipitation over land from: (a) IMERGv6 (2000–2021), (b) PI E3SMv0 model (years 85–131) and (c) Their difference (model–IMERGv6). PLS regression coefficients (Equation 1) of the continental rainfall where rainfall lags by 1 month the monthly time series of (d) WS box SST (coefficient b_2); (e) WS box MLD (b_3); (f) WS box BLT (b_4); (g) ENSO3.4 (b_5); (h) IOD (b_6); and (i) the rainfall variance explained by the PLS regression fit. The hatching indicates where regression coefficients are not significant at the 95% confidence level; significance levels were evaluated using a bootstrap technique described in Text S2 in Supporting Information S1.

the north Australian monsoon dominates. The largest DJF rainfall rates in the IAAC are observed over the Indonesian archipelago, ranging from 8 to 18 mm/day. A local maximum occurs in the foothills of the New Guinea Highlands where the largest model biases (Figures 3b and 3c) are found to be more than 8 mm/day: the largest amounts of model precipitation occur on top of the mountain ridge while in the observed climatological distribution, it is south or north of the ridge. The model overestimates the northern Australian rainfall compared to the observed IMERG climatology by up to 4–5 mm/day and underestimates the rainfall over Sumatra (2–3 mm/day) and south-western Borneo (4–5 mm/day; Figure 3c).

Figures 3d–3i show the predicted rainfall patterns from the PLS regression for the case when the rainfall lags the predictors by 1 month. The maximum explained rainfall variance (Figure 3i) is ~60% over the northern part of Australia reducing to 20%–30% in the middle part of the Australian continent. Over the Indonesian Maritime Continent, there are regions in the northwest and southwest coasts of New Guinea, central New Guinea, west Sulawesi, southwestern Borneo and parts of central Java where the regression fit

explains about 35%–45% of the rainfall variance, but in the rest of the area, the prediction skill is relatively low, at about 15%–20%.

The PLS regression coefficients of the WS SST index with the Australian rainfall (Figure 3d) are most significant in the southern part of Western Australia, varying from 0.2 to 0.5 increasing southwestward from inland to the coast between 20° and 35°S. The sense of the positive correlation is that warmer SST in the WS is related to more rainfall in southwest Australia. To the north, negative regression coefficients of -0.3 are found at the tip of the Cape York Peninsula (see Figure 3a for location). Intensified rainfall here is related to cooling of the surface temperature in the WS box. The strongest relationship of the WS SST index with the Indonesian archipelago rainfall is found in Sumatra (maximum of -0.4 at the west coast), where an increase in rainfall is connected to a reduction of SST in the WS. The regression coefficients over New Guinea feature a dipole pattern, with increasing rainfall in the southern lowlands related to warmer SST west of Sumatra while the northern Papua New Guinea coastal regions show the opposite relationship.

The highest regression coefficients with the IAAC rainfall among all five of the predictors are with the WS BLT lagged by one month (Figure 3f). More than half of the Australian continental rainfall is significantly and positively correlated with the WS BLT indicating that thicker barrier layers in the WS region are related to increased rainfall. The largest regression values of 0.4–0.6 are seen in the northwest and northern parts of Australia. Although model bias is relatively high in far northern Australia (Figure 3c), the significant regression relationship between BLT and regional rainfall covers a far more extensive area (Figure 3f). Furthermore a “reverse” correlation of the monthly time series of area-averaged Australian rainfall north of 20°S with the Indo-Pacific two-dimensional distribution of the BLT highlights the WS region as having one of the highest correlations (~ 0.8) in the domain (not shown), which also supports our results. The correlations with WS BLT and rainfall in the Indonesian archipelago are lower ranging between -0.3 and 0.3. The rainfall south of $\sim 4^\circ$ S, for example, Java, southern, and central New Guinea, is positively correlated with the BLT, while to the north, it is mostly negatively correlated. This pattern is likely related to the different annual cycle regimes in these two areas with the southern area being more dominated by the Australian monsoon (Yamanaka et al., 2018).

The PLS regression patterns of the IAAC rainfall with the WS MLD (Figure 3e) have opposite signs in Indonesia and Australia. Deepening of the MLD in the WS region is related to a decrease in the Indonesian archipelago rainfall and an increase in the western and northern Australia rainfall. This relationship seems to be most significant in the areas in closest vicinity to the WS e.g., the entire Sumatra island, but overall it is not as strong as with the BLT regression coefficients.

The regression coefficients of the IAAC rainfall with the large-scale variability indices ENSO3.4 (Figure 3g) and IOD (Figure 3h) reveal much weaker correlations compared to the other regression predictors. Positive phases of ENSO3.4 relate to drier conditions in most of Australia and the southern part of New Guinea. The IOD pattern of significant regression coefficients resembles that found for the BLT (Figures 3f and 3h) but with much smaller values (0.2–0.3). The IOD is positively correlated with the rainfall in most of western and northern Australia and in the Indonesian archipelago, unexpectedly suggesting a relationship of positive IOD to the seasonal enhancement of the rainfall (Figure 3h). Indeed, a negative IOD corresponds to warm SST anomalies off Sumatra and an enhanced chance of rainfall across southern Australia, whereas a positive IOD corresponds to cooler SST anomalies off Sumatra and reduced rainfall across southern Australia (e.g., Cai et al., 2011; Risbey et al., 2009; Ummenhofer et al., 2009). The WS SST anomalies and the rainfall over Australia pattern (Figure 3d) support this finding so the positive correlation of regional rainfall (Figure 3h) with the IOD is puzzling. In fact, the isolated correlation of the Australian rainfall with IOD (at lag = 0 and leading by 1 month) as well as partial correlations with a reduced set of predictors (SST, ENSO3.4, and IOD) results in a negative correlation of the IOD with Australian rainfall as expected. The correlations become weakly positive when we include BLT in the PLS regression (Figure 3h), suggesting that there might be more complex mechanisms connecting the IOD with the WS box BLT variability that require a full-scale modeling study and so are beyond the scope of the current study. Another factor that distinguishes our study from these previous studies on IOD impact with Australian rainfall is that they were built on smoothed seasonal and annual time series, which reflects the longer term variability of IOD (Cai et al., 2011; Risbey et al., 2009; Ummenhofer et al., 2009) whereas we used an unsmoothed monthly time series on shorter time scales (i.e., on the order of months).

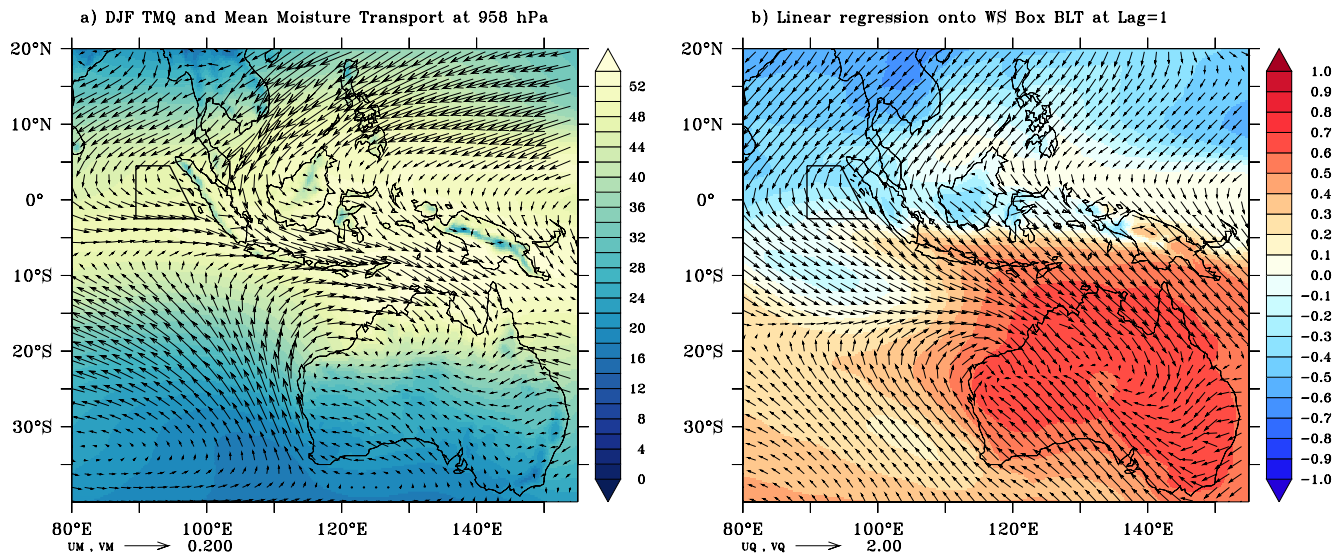


Figure 4. (a) Climatological DJF distribution from the PI E3SMv0 model (years 85–131) of total vertically integrated precipitable water (TMQ, color, kg/m²) and mean moisture transport vectors (m/s kg/kg) at 958 hPa, (b) Linear regression coefficients of monthly standardized anomalies of TMQ (color) and the multi-variate moisture transport components (vectors) at 958 hPa with the WS Box BLT after a 1-month time lag for model years 85–131.

4.1. Mechanisms of BLT Impact on the IAAC Rainfall

The proximity of the Asian continent to the northern Indian Ocean makes the regional dynamics remarkably different from other tropical oceans. In the northern Indian Ocean, the contrast in the land-ocean seasonal heating causes the reversal of the wind regime from easterly winds in the winter to westerly in the summer rather than having steady easterly trades along the equator (Schott et al., 2009; Webster et al., 1998). During the boreal winter of DJF northeasterly winds from the Asian continent blow dry cold air toward the warm Indian Ocean that converge at the equator west of Sumatra with the southeasterly winds from the southern hemisphere producing significant amounts of precipitation over the maritime continent and northern Australia (corresponding to the Australian wet monsoon season; Figures 3a and 3b, Figure S1 in Supporting Information S1).

This is consistent with the model DJF near-surface mean moisture transport pattern (Figure 4a, vectors) and the distribution of the vertically integrated total precipitable water (TMQ) (color) having the highest values over the Indonesian archipelago and northern Australia. The near surface level (958 hPa) mean moisture transport produces the largest regression coefficients of all the different vertical pressure levels, and closely follows the surface level (993 hPa) wind pattern. Linear regression of the standardized TMQ monthly time series and the multi-variate regression of the monthly standardized moisture transport components at 958 hPa with the WS BLT monthly time series at a time lag of 1 month reveals a strong positive correlation over the Australian continent with highest TMQ regression coefficient values of ~ 0.6 – 0.7 in the northern sector (Figure 4b).

The thickening of the barrier layer west of Sumatra in NDJ increases the local ocean evaporation and intensifies the local atmospheric convection (Figure 2). Subsequently, during the DJF season when the north-westerly winds are passing over the region (Figure 4), this local air–sea interaction provides an additional source of moisture for the Australasian monsoon system and intensifies the rainfall over northern Australia.

5. Conclusions

This study aims to understand the role of the local barrier layer in the eastern Indian Ocean on air–sea interaction and its subsequent impact on the continental rainfall over the Indonesian archipelago and Australia. We focus on a region west of Sumatra, where the BLT has a local maximum in NDJ. Our findings support our hypothesis that there is a strong correlation between the barrier layer thickness in this region and the

rainfall over the IAAC. In particular, enhanced BLT in the WS relates to increased rainfall over northern Australia. The regression patterns are more complex over the Indonesian archipelago, where the rainfall in regions south of 4°S is mostly positively correlated while north of 4°S, the correlations are mostly negative. This is likely due to the different types of seasonal cycles in rainfall over these areas: the southern areas are under the influence of the Australian monsoon, while the northern areas are more impacted by the East-Asian monsoon.

Initially, we hypothesized that the feedback mechanism by which the barrier layer amplifies atmospheric convection is by trapping the heat and warming up the SST, consequently intensifying evaporation. However, we found that the thickest barrier layers occur during NDJ, the seasonal period of relatively low SST and reduced surface heat fluxes. Rather than by increased heating, intensified evaporation occurs due to stronger wind forcing. The barrier layer limits the penetration depth of the wind mixing and thus additionally intensifies the turbulent mixing heat flux, causing surface ocean heat loss via evaporation (increased latent heat flux) and conduction (increased sensible heat flux). Furthermore, during the maximum BLT season during NDJ the intensified production of surface moisture is delivered to the upper atmospheric levels via increased atmospheric convection (as evident in the OLR decrease during this time). Therefore, the BLT in the WS region serves as a mechanism for amplification of the monsoon moisture that is transported to the Australian continent. Further evidence for this teleconnection was found in the high positive correlations of BLT with TMQ along a pathway originating from the WS carried by the southeast moisture transport toward northern Australia. Nonetheless, further investigation is needed to quantify the impact of the barrier layer on the local surface turbulent heat fluxes and the moisture fluxes in the upper atmosphere to more fully assess their contribution to the rainfall anomaly over the IAAC.

Nicholls (1989) found SST variability in central Indian Ocean (~20°S, 80°E; his Figure 6) to be highly correlated to a west-east winter rainfall mode in Australia, whereas we have identified regional West Sumatra BLT variability to be highly correlated with a north-south Australian rainfall pattern. Interestingly in our linear regression of the moisture transport with the WS box BLT (Figure 4b), albeit for all months, this central Indian Ocean region is located in a zonal convergence of north-westerly with south-easterly moisture flows, resulting in a pathway of eastward zonal moisture transport toward Western Australia which would affect the rainfall there.

Our analysis shows a heretofore unrealized potential predictive power of salinity stratification on regional rainfall. Specifically, the predictability skills of the WS BLT for the IAAC rainfall were investigated using a PLS regression fit of monthly time series of WS box BLT, SST, MLD, as well as the large-scale variability indices Niño3.4 and IOD to the IAAC continental rainfall. The highest correlation with the continental rainfall is with the WS box-averaged BLT at a lag of one month. Thickening of the barrier layer in the West Sumatra region is related to intensify rainfall over the northern Australia one month later. This result suggests that the BLT in the WS region possesses rainfall predictability skills and may be used as an indicator (predictor) of intensified rainfall over northern Australia.

Data Availability Statement

GPM IMERGv6 monthly data are available at https://disc.gsfc.nasa.gov/datasets/GPM_3IMERGM_06/summary?keywords=%22IMERG%20final%22. Argo data were collected and made freely available by the International Argo Program and the national programs that contribute to it (<http://www.argo.ucsd.edu>). The Argo Program is part of the Global Ocean Observing System. The AMSR-2 data (www.remss.com) are produced by Remote Sensing Systems and were sponsored by the NASA AMSR-E Science Team and the NASA Earth Science MEaSUREs Program. The Scatterometer Climatology of Ocean Winds (SCOW) is available at <https://chapman.ceoas.oregonstate.edu/scow/>. The data and model output used in this study (Ivanova et al., 2021) are freely available at the DOI <https://doi.org/10.6075/J0MC8ZW3>.

Acknowledgments

D. Ivanova, J. McClean, and J. Sprintall acknowledge NASA Award NNX-13AO38G. D. Ivanova and J. McClean acknowledge U.S. DOE Office of Science/BER Grant DE-SC0012778. J. Sprintall was also supported through NOAA NA17OAR4310257 and NSF 1851316. R. Chen acknowledge the support by the National Natural Science Foundation of China (42076007). Computing resources at the Oak Ridge Leadership Computing Facility (Oak Ridge National Laboratory) were used to analyze the model output.

References

Abram, N., Henley, B. J., Sen Gupta, A., Lippmann, T. J. R., Clarke, H., Dowdy, A. J., et al. (2021). Connections of climate change and variability to large and extreme forest fires in southeast Australia. *Communications Earth & Environment*, 2, 8. <https://doi.org/10.1038/s43247-020-00065-8>

Aldrian, E., & Susanto, R. D. (2003). Identification of three dominant rainfall regions within Indonesia and their relationship to sea surface temperature. *International Journal of Climatology*, 23, 1435–1452. <https://doi.org/10.1002/joc.950>

Cai, W., van Rensch, P., Cowan, T., & Hendon, H. (2011). Teleconnection pathways of ENSO and the IOD and the mechanisms for impacts on Australian rainfall. *Journal of Climate*, 24, 3910–3923. <https://doi.org/10.1175/2011jcli4129.1>

Chang, C.-P., Lu, M.-M., & Lim, H. (2016). Monsoon convection in the maritime continent: Interaction of large-scale motion and complex terrain. *Meteorological Monographs*, 56, 6.1–6.29. <https://doi.org/10.1175/amsmonographs-d-15-0011.1>

Chernick, M. R. (2011). *Bootstrap methods: A Guide for Practitioners and Researchers* (Vol. 619). John Wiley & Sons.

Chi, N.-H., Lien, R.-C., D'Asaro, E. A., & Ma, B. B. (2014). The surface mixed layer heat budget from mooring observations in the central Indian Ocean during Madden-Julian Oscillation events. *Journal of Geophysical Research: Oceans*, 119, 4638–4652. <https://doi.org/10.1002/2014jc010192>

Choudhury, D., Sen Gupta, A., Sharma, A., Taschetto, A. S., Mehrotra, R., & Sivakumar, B. (2017). Impacts of the tropical trans-basin variability on Australian rainfall. *Climate Dynamics*, 49, 1617–1629. <https://doi.org/10.1007/s00382-016-3405-z>

Drushka, K., Sprintall, J., & Gille, S. T. (2014). Subseasonal variations in salinity and barrier-layer thickness in the eastern equatorial Indian Ocean. *Journal of Geophysical Research*, 119, 805–823. <https://doi.org/10.1002/2013jc009422>

Durack, P. J., & Wijffels, S. E. (2010). Fifty-year trends in global ocean salinities and their relationship to broad-scale warming. *Journal of Climate*, 23, 4342–4362. <https://doi.org/10.1175/2010jcli3377.1>

Felton, C. S., Subrahmanyam, B., Murty, V. S. N., & Shriver, J. F. (2014). Estimation of the barrier layer thickness in the Indian Ocean using Aquarius Salinity. *Journal of Geophysical Research: Ocean*, 119, 4200–4213. <https://doi.org/10.1002/2013jc009759>

Freund, M., Henley, B. J., Karoly, D. J., Allen, K. J., & Baker, P. J. (2017). Multi-century cool- and warm-season rainfall reconstructions for Australia's major climatic regions. *Climate of the Past*, 13, 1751–1770. <https://doi.org/10.5194/cp-13-1751-2017>

Graham, N. E., & Barnett, T. P. (1987). Sea surface temperature, surface wind divergence, and convection over tropical oceans. *Science*, 238, 657–659. <https://doi.org/10.1126/science.238.4827.657>

Hamada, J. I., Yamanaka, M. D., Matsumoto, J., Fukao, S., Winarso, P. A., & Sribimawati, T. (2002). Spatial and temporal variations of the rainy season over Indonesia and their link to ENSO. *Journal of Meteorological Society of Japan*, 80, 285–310. <https://doi.org/10.2151/jmsj.80.285>

Hendon, H. H. (2003). Indonesian rainfall variability: Impacts of ENSO and local air-sea interaction. *Journal of Climate*, 16, 1775–1790. [https://doi.org/10.1175/1520-0442\(2003\)016<1775:irvioe>2.0.co;2](https://doi.org/10.1175/1520-0442(2003)016<1775:irvioe>2.0.co;2)

Hidayat, R., Ando, K., Masumoto, Y., & Luo, J. J. (2016). Interannual variability of rainfall over Indonesia: Impacts of ENSO and IOD and their predictability. *IOP Conference Series of Earth Environmental Science*, 31, 012043. https://doi.org/10.1142/9789814343411_0006

Huffman, G. J., Stocker, E. F., Bolvin, D. T., Nelkin, E. J., & Tan, J. (2019). *GPM IMERG final precipitation L3 1 month 0.1 degree x 0.1 degree V06, Greenbelt, MD*. Goddard Earth Sciences Data and Information Services Center (GES DISC). <https://doi.org/10.5067/GPM/IMERG/3B-MONTH/06>

Hurrell, J. W., Hack, J. J., Shea, D., Caron, J. M., & Rosinski, J. (2008). A new sea surface temperature and sea ice boundary dataset for the Community Atmosphere Model. *Journal of Climate*, 21, 5145–5153. <https://doi.org/10.1175/2008jcli2292.1>

Ivanova, D. P., McClean, J. L., Sprintall, J., & Chen, R. (2021). *Data from: The oceanic barrier layer in the eastern Indian Ocean as a predictor for rainfall over Indonesia and Australia*. UC San Diego Library Digital Collections. <https://doi.org/10.6075/10MC8ZW3>

Kay, J. E., Hillman, B. R., Klein, S. A., Zhang, Y., Medeiros, B., Pincus, R., et al. (2012). Exposing global cloud biases in the Community Atmosphere Model (CAM) using satellite observations and their corresponding instrument simulators. *Journal of Climate*, 25, 5190–5207. <https://doi.org/10.1175/jcli-d-11-00469.1>

Krishnamohan, K., Vialard, J., Lengaigne, M., Masson, S., Samson, G., Pous, S., et al. (2019). Is there an effect of Bay of Bengal salinity on the northern Indian Ocean climatological rainfall? *Deep-Sea Research Part II*, 166, 19–33. <https://doi.org/10.1016/j.dsr2.2019.04.003>

Large, W. G., McWilliams, J. C., & Doney, S. C. (1994). Oceanic vertical mixing: A review and a model with a nonlocal boundary layer parameterization. *Reviews of Geophysics*, 32(4), 363–403. <https://doi.org/10.1029/94rg01872>

Large, W. G., & Yeager, S. G. (2009). The global climatology of an interannually varying air-sea flux data set. *Climate Dynamics*, 33, 341–364. <https://doi.org/10.1007/s00382-008-0441-3>

Li, J., Liang, C., Tang, Y., Dong, C., Chen, D., Liu, X., & Jin, W. (2016). A new dipole index of the salinity anomalies of the tropical Indian Ocean. *Scientific Reports*, 6, 1–10. <https://doi.org/10.1038/srep24260>

Li, L., McClean, J. L., Miller, A. J., Eisenman, I., Hendershott, M. C., & Papadopoulos, C. A. (2014). Processes driving sea ice variability in the Bering Sea in an eddying ocean/sea ice model: Mean seasonal cycle. *Ocean Modelling*, 84, 51–66. <https://doi.org/10.1016/j.ocemod.2014.09.006>

Li, L., Schmitt, R. W., Ummenhofer, C. C., & Karnauskas, K. B. (2016a). Implications of North Atlantic sea surface salinity for summer precipitation over the US Midwest: Mechanisms and predictive values. *Journal of Climate*, 29, 3143–3159. <https://doi.org/10.1175/jcli-d-15-0520.1>

Li, L., Schmitt, R. W., Ummenhofer, C. C., & Karnauskas, K. B. (2016b). North Atlantic salinity as a predictor of Sahel rainfall. *Science Advances*, 2, e1501588. <https://doi.org/10.1126/sciadv.1501588>

Li, Y., Han, W., Wang, W., Ravichandran, M., Lee, T., & Shinoda, T. (2017). Bay of Bengal salinity stratification and Indian summer monsoon intraseasonal oscillation: 2. Impact on SST and convection. *Journal of Geophysical Research: Oceans*, 122, 4312–4328. <https://doi.org/10.1002/2017jc012692>

Mahadevan, A., Spiro Jaeger, G., Freilich, M., Omand, M., Shroyer, E. L., & Sengupta, D. (2016). Freshwater in the Bay of Bengal: Its fate and role in air-sea heat exchange. *Oceanography*, 29(2), 72–81. <https://doi.org/10.5670/oceanog.2016.40>

Maltrud, M. E., Bryan, F. O., & Peacock, S. (2010). Boundary impulse response functions in a century-long eddying global ocean simulation. *Environmental Fluid Mechanics*, 10(1–2), 275–295. <https://doi.org/10.1007/s10652-009-9154-3>

Masson, S., Delecluse, P., Boulanger, J.-P., & Menkes, C. (2002). A model study of the seasonal variability and formation mechanisms of the barrier layer in the eastern equatorial Indian Ocean. *Journal of Geophysical Research: Oceans*, 107, SRF 18–1–SRF 18–20. <https://doi.org/10.1029/2001jc000832>

McClean, J. L., Bader, D. C., Maltrud, M. E., Evans, K. J., Taylor, M. A., Tang, Q., et al. (2018). High-resolution fully-coupled ACME v0.1 approximate present day transient climate simulations. In *Ocean Sciences Meeting 2018*.

- Meehl, G. A., Yang, D., Arblaster, J. M., Bates, S., Rosenbloom, N., Neale, R., et al. (2019). Effects of model resolution, physics, and coupling on Southern Hemisphere storm tracks in CESM1.3. *Geophysical Research Letters*. <https://doi.org/10.1016/j.pocan.2009.03.004>
- Meyers, G., McIntosh, P., Pigot, L., & Pook, M. (2007). The years of El Niño, La Niña and interactions with the tropical Indian Ocean. *Journal of Climate*, 20, 2872–2880. <https://doi.org/10.1175/jcli4152.1>
- Neale, R., & Slingo, J. (2003). The Maritime Continent and its role in the global climate: A GCM study. *Journal of Climate*, 16, 8342–8848. [https://doi.org/10.1175/1520-0442\(2003\)016<0834:tmcair>2.0.co;2](https://doi.org/10.1175/1520-0442(2003)016<0834:tmcair>2.0.co;2)
- Nicholls, N. (1989). Sea surface temperatures and Australian winter rainfall. *Journal of Climate*, 2, 965–973. [https://doi.org/10.1175/1520-0442\(1989\)002<0965:sstaaw>2.0.co;2](https://doi.org/10.1175/1520-0442(1989)002<0965:sstaaw>2.0.co;2)
- Park, S., Bretherton, C. S., & Rasch, P. J. (2014). Integrating cloud processes in the community atmosphere model, Version 5. *Journal of Climate*, 27, 6821–6856. <https://doi.org/10.1175/jcli-d-14-00087.1>
- Pujiana, K., & McPhaden, M. J. (2018). Ocean surface layer response to convectively coupled Kelvin waves in the eastern equatorial Indian Ocean. *Journal of Geophysical Research: Oceans*, 123, 5727–5741. <https://doi.org/10.1029/2018jc013858>
- Qiu, Y., Cai, W., Li, L., & Guo, X. (2012). Argo profiles variability of barrier layer in the tropical Indian Ocean and its relationship with the Indian Ocean Dipole. *Geophysical Research Letters*, 39. <https://doi.org/10.1029/2012gl015441>
- Rathore, S., Bindoff, N. L., Ummenhofer, C. C., Phillips, H. E., & Feng, M. (2020). Near-surface salinity reveals the oceanic sources of moisture for Australian precipitation through atmospheric moisture transport. *Journal of Climate*, 33, 6707–6730. <https://doi.org/10.1175/jcli-d-19-0579.1>
- Risbey, J. S., Pook, M. J., McIntosh, P. C., Wheeler, M. C., & Hendon, H. H. (2009). On the remote drivers of rainfall variability in Australia. *Monthly Weather Review*, 137, 3233–3253. <https://doi.org/10.1175/2009mwr2861.1>
- Risien, C. M., & Chelton, D. B. (2008). A global climatology of surface wind and wind stress fields from eight years of QuikSCAT Scatterometer Data. *Journal of Physical Oceanography*, 38, 2379–2413. <https://doi.org/10.1175/2008jpo3881.1>
- Robertson, A. W., V. Moron, J.-H. Qian, C.-P. Chang, F. Tangang, E. Aldrian, et al. (2011). The maritime continent monsoon. In C.-P. Chang (Ed.), *The global monsoon system research and forecast* (pp. 85–98). World Scientific Publication Company.
- Roemmich, D., & Gilson, J. (2009). The 2004–2008 mean and annual cycle of temperature, salinity, and steric height in the global ocean from the Argo Program. *Progress in Oceanography*, 82, 81–100. <https://doi.org/10.1088/1755-1315/31/1/012043>
- Rosipal, R., & Kramer, N. (2006). Overview and Recent Advances in Partial Least Squares. In *SLSFS'05 Proceedings of the 2005 International Conference on Subspace, Latent Structure and Feature Selection* (pp. 34–51). Springer-Verlag.
- Saji, N. H., Goswami, B. N., Vinayachandran, P. N., & Yamagata, T. (1999). A dipole mode in the tropical Indian Ocean. *Nature*, 401, 360–363. <https://doi.org/10.1038/43854>
- Schott, F. A., Xie, S.-P., & McCreary, J. P., Jr. (2009). Indian Ocean circulation and climate variability. *Reviews of Geophysics*, 47, 1–46. <https://doi.org/10.1029/2007rg000245>
- Sperber, K. R., Annamalai, H., Kang, I. S., Kitoh, A., Moise, A., Turner, A., et al. (2013). The Asian summer monsoon: An intercomparison of CMIP5 vs. CMIP3 simulations of the late 20th century. *Climate Dynamics*, 41(9–10), 2771–2744. <https://doi.org/10.1007/s00382-012-1607-6>
- Sprintall, J., & Roemmich, D. (1999). Characterizing the structure of the surface layer of the Pacific Ocean. *Journal of Geophysical Research*, 104, 23297–23311. <https://doi.org/10.1029/1999jc000179>
- Sprintall, J., & Tomczak, M. (1992). Evidence of the barrier layer in the surface layer of the tropics. *Journal of Geophysical Research*, 97, 7305. <https://doi.org/10.1029/92jc00407>
- Taschetto, A. S., Sen Gupta, A., Hendon, H. H., Ummenhofer, C. C., & England, M. H. (2011). The contribution of Indian Ocean sea surface temperature anomalies on Australian summer rainfall during EL Niño events. *Journal of Climate*, 24, 3734–3747. <https://doi.org/10.1175/2011jcli3885.1>
- Trenberth, K. E. (1997). The definition of El Niño. *Bulletin of the American Meteorological Society*, 78, 2771–2777. [https://doi.org/10.1175/1520-0477\(1997\)078<2771:tdoeno>2.0.co;2](https://doi.org/10.1175/1520-0477(1997)078<2771:tdoeno>2.0.co;2)
- Ummenhofer, C. C., England, M. H., McIntosh, P. C., Meyers, G., Pook, M. J., Risbey, J. S., et al. (2009). What causes southeast Australia's worst droughts? *Geophysical Research Letters*, 36, L04706. <https://doi.org/10.1029/2008gl036801>
- van Oldenborgh, G., Krikken, F., Lewis, S., Leach, N. J., Lehner, F., Saunders, K. R., et al. (2020). Attribution of the Australian bushfire risk to anthropogenic climate change. *Natural Hazards and Earth System Sciences*. <https://doi.org/10.5194/nhess-2020-69>
- Vinayachandran, P. N., & Shetye, S. R. (1991). The warm pool in the Indian Ocean. *Proceedings of the Indian Academy of Sciences—Earth & Planetary Sciences*, 100, 165–175. <https://doi.org/10.1007/BF02839431>
- Webster, P. J., Magaña, V. O., Palmer, T. N., Shukla, J., Tomas, R. A., Yanai, M., & Yasunari, T. (1998). Monsoons: Processes, predictability, and the prospects for prediction. *Journal Geophysical Research Ocean*, 103, 14451–14510. <https://doi.org/10.1029/97jc02719>
- Wentz, F. J., Meissner, T., Gentemann, C., Hilburn, K. A., & Scott, J. (2014). *Remote sensing systems GCOM-W1 AMSR2 [monthly] environmental suite on 0.25 deg grid, version 8.2*. Remote Sensing Systems. Retrieved from www.remss.com/missions/amr2
- Wheeler, M. C., Hendon, H. H., Cleland, S., Meinke, H., & Donald, A. (2009). Impacts of the Madden-Julian oscillation on Australian rainfall and circulation. *Journal of Climate*, 22, 1482–1498. <https://doi.org/10.1175/2008jcli2595.1>
- Yamanaka, M. D., Ogino, S. Y., Wu, P. M., Jun-Ichi, H., Mori, S., Matsumoto, J., & Syamsudin, F. (2018). Maritime continent coastlines controlling Earth's climate. *Progress in Earth and Planetary Science*, 5. <https://doi.org/10.1186/s40645-018-0174-9>

Reference From the Supporting Information

- Thomson, R. E., & Emery, W. J. (2014). *Data analysis methods in physical oceanography* (3rd ed.). Elsevier.